Volume 8
Number 2
14 January 2020
Pages 179–344

Journal of Materials Chemistry B

Materials for biology and medicine

rsc.li/materials-b

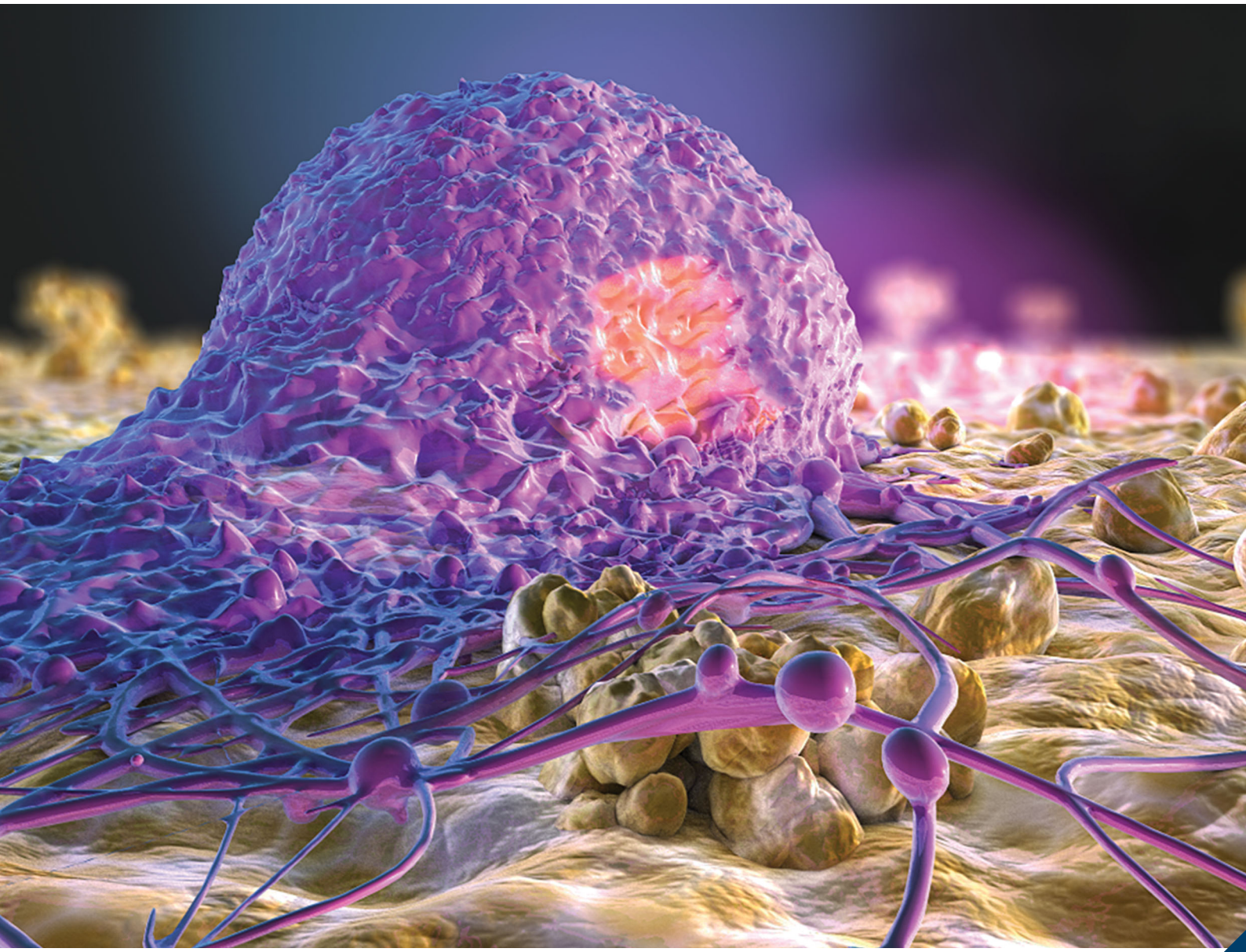

ISSN 2050-750X

ROYAL SOCIETY OF CHEMISTRY

PAPER

Alexander J. Steeves and Fabio Variola
Elucidating structure–function relationships governing the interfacial response of human mesenchymal stem cells to polydopamine coatings

Indexed in Medline!

Journal of Materials Chemistry B

PAPER

View Article Online
View Journal | View Issue

Cite this: J. Mater. Chem. B, 2020, 8, 199

Elucidating structure–function relationships governing the interfacial response of human mesenchymal stem cells to polydopamine coatings†

Alexander J. Steeves [ab] and Fabio Variola *[abcd]

Received 6th October 2019,
Accepted 10th November 2019

DOI: 10.1039/c9tb02188d

rsc.li/materials-b

Deposition of mussel-inspired polydopamine (PDA) has rapidly emerged as a simple yet effective strategy to functionalize the surface of biomaterials. The experimental simplicity of the deposition process, combined with native bioactivity and bioadhesive properties, make PDA an attractive solution for biomedical applications, ranging from functional biomaterials for tissue engineering to antibacterial surfaces. Unveiling the interplay among deposition parameters, physicochemical properties of the resulting structures and their functions, is a fundamental aspect to unlock a more sophisticated knowledge of PDA biofunctionalization and its role in controlling key biological events, such as stem cell response. Although the mechanism for the bioinductive capacity of PDA is not fully understood, surface topography, chemistry and adhesive properties are believed to play a critical role, either individually or in combination. This work addresses the differential roles of such surface properties on PDA bioactivity. We achieved novel insights on the physicochemical makeup of two PDA coatings obtained by varying one critical parameter (*i.e.*, solution agitation) during the deposition. Successively, we focused on the effects on human mesenchymal stem cells (hMSCs) in both normal and serum-free culturing conditions. This study reveals both the serum-dependent and independent cueing involved in bioactive induction caused by PDA.

Introduction

How cells sense and respond to both natural (*e.g.*, extracellular matrix) and synthetic (*e.g.*, biomaterials) substrates is still a most challenging question. The physicochemical properties of surfaces are known to induce changes in cytoskeletal organization and cellular dynamics,[1] triggering signaling pathways that ultimately determine cell fate.[2] This aspect is particularly important in bioengineering and regenerative medicine since cellular response at the biomaterial–host tissue interface ultimately dictates the biological outcome of an implanted device.[3–5] To elucidate the mechanisms involved in cell–substrate interactions and unveil the interplay between surface features (*e.g.*, topography, stiffness, chemistry) and cellular response (*e.g.*, spreading, proliferation, migration, differentiation), a variety of micro- and nano-structured surfaces with tunable properties have been employed.[6–8] The ability to control these characteristics allows for the modulation of physicochemical cueing exerted on cells, ultimately unlocking a more sophisticated knowledge of interfacial phenomena.[9] Such discoveries not only revealed new aspects of cell biology,[10] but also generated fundamental data for the rational design of functional biomaterials.[11–13] Taken together, previous work highlights the importance of closing in on specific physical and chemical factors that control cell activity to define their individual and combined contribution to changes in biological response to synthetic biomaterials, for advances of both fundamental and practical importance.

In this context, among the most promising functional biomaterials developed in the last decade, mussel-inspired polydopamine (PDA) has emerged as a simple and effective solution to control interfacial biological events. Investigation into the adhesive properties of *Mytilus edulis* mussels in aqueous environments resulted in the determination that a considerable amount of the key adhesive protein Mefp5 was composed of the amino acid L-DOPA, the precursor to dopamine (DA).[14] This insight led to the discovery that when DA is dissolved in a slightly basic buffer solution, spontaneous polymerization occurs and an adhesive polydopamine coating consisting of dopamine, quinone and 5,6-dihydroxyindole (DHI) subunits forms.[15]

[a] Faculty of Engineering, Department of Mechanical Engineering, University of Ottawa, Canada. E-mail: fabio.variola@uottawa.ca
[b] Ottawa-Carleton Institute for Biomedical Engineering, Ottawa, Canada
[c] Faculty of Medicine, Department of Cellular and Molecular Medicine, University of Ottawa, Canada
[d] Children's Hospital of Eastern Ontario (CHEO), Ottawa, ON, Canada

† Electronic supplementary information (ESI) available. See DOI: 10.1039/c9tb02188d

The adhesive characteristics of the polymer enables it to be effectively deposited on a wide range of organic and inorganic substrates.[16] As a result, PDA has been largerly exploited to immobilize bioactive agents (*e.g.*, antibiotics, bioactive proteins) in order to endow biomaterials with novel properties, such as the capacity to limit bacterial adhesion and to enhance cellular functions.[16,17] However, despite the majority of studies has utilized PDA as an intermediate linker and/or combined with other materials in composites,[18–20] it possesses intrinsic antibacterial and bioactive abilities.[21] A recent study employed rotation during deposition to generate a PDA surface that displayed elevated intrinsic antibacterial activity against Gram-positive and Gram-negative bacteria, with bactericidal ratios of 90–99% in comparison to the $<5\%$ of classically deposited PDA. The study confirmed the presence of a roughened surface (rPDA) resulting from the accumulation of multi-scale PDA particles and aggregates capable of exerting contact-kill antibacterial effects while still providing a viable substrate for HeLa cells.[22] In addition, PDA has been shown to provide enhancement of endothelial cell adhesion and viability of electrospun polycaprolactone (PCL) nanofibers[23] as well as the ability to reduced toxicity of a variety of nanomaterials.[24–26] In this context, it is suggested that bioinductive effects of PDA may be associated with its ability to prevent denaturation of adsorbed serum protein and/or enhance specific protein immobilization.[27] Proteins adsorption on surfaces is believed to play a critical role in determining the fate of the subsequent cell colonization.[28] However, previous work on PDA from our group determined no significant correlation between the ability to affect serum protein adsorption and the substantial enhancement of MG-63 osteoblastic cell adhesion and proliferation.[29] In an effort to identify the specific physicochemical factors that determine the bioactivity of PDA, and in particular the implications of its adhesive properties in protein adsorption, we carried out a comprehensive investigation of structure–function relationships with two PDA coatings obtained by varying one critical parameter (*i.e.*, solution agitation) during the deposition. To this end, we employed a wide array of advanced characterization techniques to investigate the physical, chemical and nanomechanical properties of PDA. Successively, we focused on the response of human mesenchymal stem cells (hMSCs), a multipotent cell line widely used due to their ability to differentiate into a variety of terminal cells types upon physicochemical cueing and the growing interest for a variety of future therapeutic treatments.[30–33]

Results from this study demonstrate that the simple employment of rotation during deposition generates a PDA surface that, in addition to possessing antibacterial properties,[22] is also characterized by significant enhancements of hMCS bioactivity in both normal and serum-starved culturing conditions. We also show that the surface works synergistically with dissolved and preadsorbed serum proteins, supporting the hypothesis that PDA possesses lone physicochemical cues that work in concert with the environment to elicit its advantageous effects. In conclusion, our study provides new insights into the bioinductive mechanism of action for PDA while providing additional evidence to support the use of rPDA as a functional coating for applications in bioengineering and regenerative medicine.

Materials and methods

Sample preparation of sPDA and rPDA coatings

12 mm borosilicate glass coverslips (#1.5, Fisher Scientific, USA) were ultrasonically cleaned in toluene and rinsed with distilled water (DI). Samples were separated into three batches for the subsequent PDA deposition *via* a 24 h treatment. Control batch (*i.e.*, bare glass coverslips) was immersed in 1× PBS (Corning, USA). The two remaining batches were immersed in a freshly prepared 2 mg mL^{-1} solution of dopamine–HCl (Sigma-Aldrich, USA) in 25 mM Tris–HCl (pH = 8.6, Sigma-Aldrich), according to a previously published protocol.[14] For one of the two batches, named hereafter sPDA (where "s" stands for static), PDA was deposited in stationary conditions (*i.e.*, no agitation), following the original deposition methodology.[14] For the second batch, named hereafter rPDA (where "r" stands for rotation), PDA was deposited while the beaker containing the glass substrates immersed in the PDA solution was in motion on a shaking platform at 200 rpm.[22] Beakers were placed on a Styrofoam block to prevent even minimal heat transfer from the shaking platform. Coated samples were successively rinsed with DI and dried in air.

To investigate the effects of serum-protein pre-adsorption, each batch of samples was further separated into three conditions (control, CTRL; no pre-adsorption, NPA; pre-adsorption, PA) for the overnight incubation. In particular, the CTRL condition was incubated in 1× PBS. Conversely, Dulbecco's Modified Eagle Medium (DMEM, Corning), without additives (*e.g.*, antibiotics), was used as the base medium for the remaining conditions. The NPA condition involved incubation in unmodified DMEM. The PA condition involved incubation in DMEM enriched with 8% Fetal Bovine Serum (FBS, Thermo Fisher, USA). After incubation, all surfaces were rinsed with DI water and stored in 1× PBS.

Scanning electron microscopy (SEM)

SEM imaging was carried out with a JSM-7500 Field Emission Scanning Electron Microscope (FESEM, JEOL, Japan). SEM was used to visualize control and PDA-coated surfaces, as well as adherent hMSCs after 24 h of culture. Micrographs were imported into Fiji (ImageJ) and the major axis of each aggregate was manually measured.[34,35]

Atomic force microscopy (AFM)

Atomic force microscopy (AFM) analysis was carried out with an alpha300 RSA system (WITec, Germany). This AFM is capable of multiple modes including the non-resonant, intermittent-contact Digital Pulsed Force Mode (DPFM) and Non-Contact (NC) mode. Source files were imported into Gwyddion (http://gwyddion.net/) and processed to generate 3D-surface projections, calculated *via* the triangulation method between neighboring pixels, which were subsequently used to measure surface area (SA) and roughness (RMS).[36]

Topographical imaging and quantification of nanomechanical properties were carried out in DPFM mode. Of note, in order to prevent noise from unspecific tip–surface interactions, NC-AFM mode was specifically used to image the inter-aggregate space. Triangular Si_3N_4 Cantilever C of the DNP-S chip (Bruker, USA) and the rectangular cantilever of the RFESPA-40 chip (Bruker), were used for DPFM and NC, respectively. The former is characterized by a rotated pyramidal tip with a nominal radius of 10 nm, spring constant of 0.24 N m^{-1} and nominal frequency of 56 kHz. The latter is characterized by a rotated pyramidal tip with a nominal radius of 8 nm, resonant frequency of 40 kHz and spring constant of 0.9 N m^{-1}. In the case of DPFM measurements, each 6 × 6 μm image provides 2.6 × 10^5 force distance curves. 40 curves were selected from inter-aggregate regions as well as from individual aggregates, in a relative proportion and analyzed to extract nanomechanical parameters. To this end, the force–distance curves were converted from deflection [V]-phase [φ] (AFM output) into force [N]-indentation depth [nm] according to a previously published procedure.[37] From these curves, we calculated the stiffness, Young's modulus adhesion force, detachment energy, hardness, compliance and hysteresis.[37] To quantify Young's modulus, the Derjaguin–Muller–Toporov (DMT) model was used due to its applicability to soft materials when adhesive forces are present.[38]

X-ray photoelectron spectroscopy (XPS)

The surface chemistry of deposited PDA coatings was assessed by a XSAM-800 X-ray Photoelectron Spectroscope (Kratos, Japan). A wide-scan survey spectrum was recorded to visualize the elemental composition of the surface, which was successively analyzed by CasaXPS software (CASA Software Ltd, UK). Investigation was performed in the 279–291 eV, 389–407 eV and 522–540 eV regions which identify carbon (C 1s), oxygen (O 1s) and nitrogen (N 1s). Curve fitting for specific chemical groups was done through OriginPro (Origin Labs Corp., USA) with insight into peak deconvolution and fitting in line with previous literature.[39]

Raman spectroscopy

Spectroscopic analysis was carried with the Raman module of the alpha300 RSA system to ensure homogenous PDA deposition across the surface of the cover slip. 10 × 10 μm Raman maps were collected through a 100× Objective (EC Epiplan NEOFLUAR, N.A. = 0.9, Zeiss, Germany) at high resolution (100 × 100 points) with a 785 nm Toptica XTRA Laser (Germany, 40 mW, acquisition time = 0.2 s) as the excitation source. Representative spectra were collected using a similar hardware configuration with 10 mW laser power and an integration time of 30 seconds over 6 acquisitions. Analysis of Raman bands in the 250–3000 cm^{-1} range was carried out by using the Project 4 PLUS (WITec) and OriginPro, capitalizing on previous literature for peak assignment.[29,40–42]

Contact angle goniometry

The static water contact angle was measured with a VCA Optima Surface Analysis System (AST Products Inc., USA) after samples were rinsed and vacuum dried for 16 h. A (1 μL) drop of deionized water was ejected from a micro syringe (Hamilton Company, USA), picture taken and a manual outline of key points of the droplet was performed to ensure accuracy prior to automated measurement of the angle. Three droplets were measured for each sample, and experiments were carried out in triplicate, for a total of nine contact angle measurements per condition.

Cell culture

Three sources of bone-marrow derived human mesenchymal stem cells (hMSCs) were obtained from two distributors (Lonza, USA and RoosterBio, USA) to account for donor variability. hMSCs from RoosterBio (Lot. 00014; Lot. 00082) were expanded in High Performance Media (RoosterBio) and were thawed in similar media. hMSCs from Lonza (Lot. 603525) were expanded in Mesenchymal Stem Cell Growth Medium BulletKit (MSCGM, Lonza) and were thawed in similar media. Subsequent experimental culturing was performed in DMEM with 4.5 g L^{-1} glucose and L-glutamine (Corning, USA), supplemented with 8% fetal bovine serum (FBS, Gibco, USA), 100 U mL^{-1} penicillin and 100 μg mL^{-1} streptomycin (Gibco). The culture was maintained in a 5% CO_2, 37 °C water-jacketed incubator. Cells were passaged with 1× TrypLE (Gibco). To ensure the complete neutralization of the trypsin enzyme, 50 μg mL^{-1} Soybean Trypsin Inhibitor (Sigma-Aldrich) was used and added for 5 min. Cells were collected and centrifuged at 190*g* for 8 minutes. Successively, the supernatant was discarded, and pellet reconstituted in fresh culture media to desired concentrations specific to the experiment to a total volume of 500 μL per well. Incubation periods thereafter were dependent on each experiment.

All experiments in this work were repeated in triplicate with at least three samples/condition. Bar charts are expressed as the mean with standard deviation (SD). Data sets were tested for normality using the Shapiro–Wilk test. Normal data sets were tested with the parametric two-way ANOVA with Tukey's HSD *post hoc* test for mean comparisons. A difference was considered significant if $P < 0.05$. Statistical significance was defined as $*P < 0.05$ and $**P < 0.01$. Analyses were performed with GraphPad Prism 8 (GraphPad Software, Inc.) and OriginPro.

Cellular imaging: immunofluorescence and SEM

After incubation at different experimental intervals, cells were fixed at room temperature with 4%-PFA for 10 minutes, washed with 1× PBS and permeabilized with 0.25% Triton-X100 (Sigma-Aldrich) for 10 minutes. Nuclei were stained with NucBlue ReadyProbes (Thermo Fisher) and the actin cytoskeleton was stained *via* Rhodamine conjugated Phalloidin (Thermo Fisher). To visualize the focal adhesions, we labeled Vinculin with a 1 : 400 mouse monoclonal Anti-hVIN1 (Sigma-Aldrich) as the primary antibody and 1 : 600 Goat anti-Mouse IgG conjugated to Alexa Fluor 488 (Thermo Fisher) as the secondary antibody.

Multi-channel images were captured with an AxioObserver.Z1 inverted microscope (Zeiss) fitted with the Zeiss Filter Set 49 (Hoechst), Chroma Filter Set 49002 (GFP) and Chroma Filter Set

49005 (Rhodamine). Low-magnification tiles of the surfaces were imaged with a 10× A-Plan (Ph2) Objective (NA = 0.25, Zeiss) for assessment of cell proliferation. Mid-magnification tiles of the surfaces were imaged with a 20× Plan-Apo (Ph2, DIC II) Objective (NA = 0.8, Zeiss) for assessment of general morphology and cell spreading. High-magnification tiles of the surface were imaged with a 40× Plan-Apo Corr. (DIC III) Objective (NA = 0.95, Zeiss) for high resolution imaging of advanced cell structure. Focal adhesions were visualized through a 40× PL APO 1.3 Oil objective (Zeiss) affixed to a Leica BMI16000B inverted microscope (Leica Microsystems, Germany), configured with a Quorum Spinning-disk Confocal (Quorum Technologies, Canada) and complemented by a Photometrics Prime BSI sCMOS [95% QE, back illuminated]. The imaging system was driven by MetaMorph Software (Molecular Devices, USA).

Image collections were stitched together with AxioVision Mosaix Software (Zeiss) and focus stacked with the Fiji distribution of ImageJ (NIH).[34,35] For the relative quantification of morphology distribution, 250 cells per condition, randomly selected from immunofluorescence images, were individually classified in 6 bins corresponding to different morphologies (*i.e.*, spherical, circular, protrusive, elongated, multipodal, multipolar) according to visual assessment based on well-defined and consistent sorting criteria.

For the quantification of cell morphology (*i.e.*, area, perimeter, form factor) and proliferation, multiple custom pipelines were created in CellProfiler.[43] These were constantly calibrated for the images to ensure quality control of results. Three main measurements were scrutinized for the cell structure, namely cell area, perimeter and form factor. Cell area was calculated by counting the scaled number of pixels within the identified cells. Perimeter was calculated by measuring the number of pixels around the boundary of the identified cell periphery. Form factor, calculated as $4 \times \pi \times (\text{area}/\text{perimeter}^2)$, is the measure of a cell circularity: a value of 1 is representative of a perfectly circular cell while 0 indicates a linear cell. Quantification of focal adhesions was achieved by using a custom macro in ImageJ that performed background subtraction, thresholding and particle analysis. Statistical analysis performed in OriginPro.

For SEM imaging, cells were fixed with a mixture of a 1%-glutaraldehyde (Grade 1, Sigma-Aldrich, G7526)/4%-paraformaldehyde for 1 h at room temperature. Samples were successively rinsed with DI and subjected to a six-step dehydration series in ethanol (EtOH) from 50% to 100%. To reduce charging effects of the organic PDA film and cells, samples were coated with a 5 nm gold (Au) film *via* Q105R Rotary-Pumped Sputterer (Quorum, Canada) prior to imaging.

Results and discussion

Morphology and nanomechanical properties

Scanning Electron (SEM) and Atomic Force (AFM) microscopy were employed to visualize the micro- and nano-topographical features of the r- and s-PDA coatings. Scanning electron imaging confirmed the presence of the distinctive granular

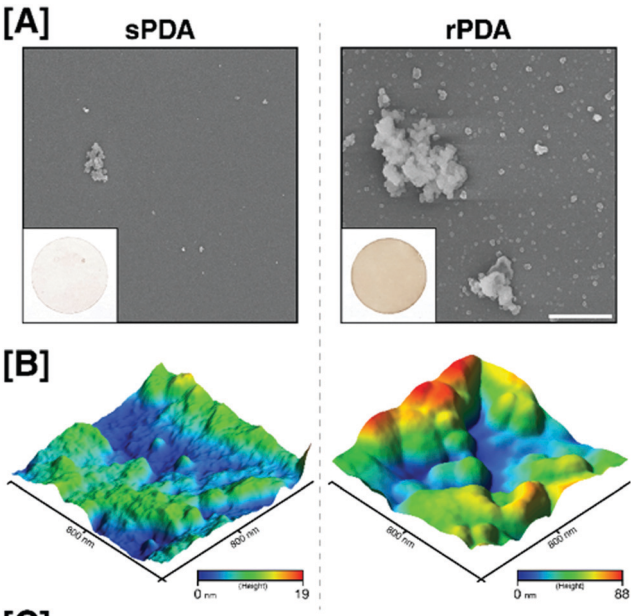

[C]

Surface	Interaggregate Region (0.75 x0.75 μm) RMS[a] (nm)	Interaggregate Region (0.75 x0.75 μm) Surface Area[a] (μm²)	Global (6 x6 μm) RMS[b] (nm)	Global (6 x6 μm) Surface Area[b] (μm²)	Aggregate Structure Dia. (nm)	Aggregate Structure Height (nm)
sPDA	4.4 ± 1.4	0.57 ± 0.1	5.2 ± 2.1	36.4 ± 7.7	117 ± 57	9.6 ± 57
rPDA	20.1 ± 5.4	0.62 ± 0.2	95.6 ± 12.7	42.6 ± 8.3	901 ± 344	382 ± 116

Abbreviations: RMS, Root Mean Squared Roughness; Dia., Diameter
a Control RMS 0.4 nm and SA 0.56 μm²
b Control RMS 0.6 nm and SA 36 μm²

Fig. 1 [A] SEM and optical (inset) images of sPDA and rPDA. Scale bar = 3 μm. [B] AFM micrographs of sPDA (left) and rPDA (right). [C] Quantification of the morphological parameters.

PDA film (hereafter also referred to as inter-aggregate region) and of surface aggregates with size extending from the nano- to the micro-scale, in line with previous literature (Fig. 1A).[22,29] These aggregates were successively binned into two categories, namely small (<300 nm) and large (>300 nm) structures, according to their major axis quantified *via* image analysis software. The small aggregates on rPDA (average major axis of 232 nm) were found to be 70% larger than those on sPDA (average major axis of 136 nm in width), with relatively low statistical deviation indicating a narrower size distribution. This trend was also confirmed for the second size category, in which the larger structures were 131% larger on rPDA (1726 *vs.* 743 nm in major axis). However, in this case, the statistical deviation was found to be substantial, suggesting that the formation of these larger aggregates is inherently stochastic and unpredictable.

While the mechanism of aggregate formation is still unknown, solvent choice and generation of a local increase in temperature due to stirring allowed us to create two morphologically-distinct PDA surfaces. In fact, it has been determined that the choice of Tris as the reaction solvent generates aggregates of larger size, when compared to other common solvents (*e.g.*, NaOH).[44] In our study, we used a 2.5 times larger Tris–HCl concentration (25 mM) than that routinely adopted for PDA coating in order to elicit the formation of larger aggregates.[22] In addition, the generation of

local heat through shaking may have contributed to determining the final size of aggregates. In fact, despite the interplay between temperature and aggregates formation is unknown, previous work has showed that increased environmental heat and the method of deposition (static, shaking, stirring) can rapidly affect the deposition kinetics of PDA films.[45] We can thus infer that the larger aggregates in the rPDA surface derive from the combination of a higher Tris concentration and the presence of stirring.

In order to further analyze the morphological features of PDA surfaces, we employed AFM imaging to visualize the three-dimensional topography of both the inter-aggregate regions and the individual aggregates. Non-contact (NC) AFM of the inter-aggregate regions showed that the underlying rPDA film exhibits characteristic granular nanostructures, however the rPDA aggregates displayed an irregular morphology (Fig. 1B). These structures contributed to the maximum height of these inter-aggregate rPDA structures being $>400\%$ taller than those observed on sPDA (Fig. 1C). This translates to a significant difference in the film's RMS roughness, which resulted to be $\sim$20 nm for rPDA and $\sim$4 nm for sPDA in these relatively small regions (*vs.* RMS_{CTRL} = 0.4 nm). The surface area, when compared to the control glass surface, was elevated by 1.5% and 9.9% in the sPDA and rPDA surfaces, respectively (*vs.* SA_{CTRL} = 0.56 μm^2).

DPFM-AFM imaging of larger regions was then used to close in on the structural characteristics of the aggregates, which exist at a micrometric scale though with distinct nanometric features, which is a fundamental step to understand potentially differential cueing between the PDA surfaces (Fig. 2A). In fact, it is now well-known that the size of nanometric and submicrometric protrusions dictates cellular functions ranging from adhesion to focal adhesion clustering.[46–49] The average diameter and height of aggregates on rPDA showed a $\sim$7-fold and $\sim$40-fold increase, respectively, when compared to sPDA (Fig. 1C). These structural differences contributed to the greater than eighteen times surface roughness on rPDA *vs.* in comparison to sPDA. In addition, the surface area was increased by 1.2% and 15.6% on sPDA and rPDA surfaces, respectively (*cf.* SA_{CTRL} = 36 μm^2). This considerable increase in rPDA is due to the presence of larger and more numerous micrometric aggregates, in addition to the larger globular nanoscale features found on both the aggregates and underlying surface.

The mechanical properties of soft polymeric substrates play a major role in regulating cell adhesion and proliferation. In particular, substrate stiffness has been shown to affect adhesion, spreading, proliferation and differentiation.[50–52] In order to inspect these aspects in our analysis, we capitalized on the DPFM-AFM's ability to concurrently measure a suite of substrate nanomechanical properties (*e.g.*, stiffness, hardness) and tip–surface interaction (*i.e.*, adhesion force) while acquiring topographical data. This results in high-resolution nanoscale maps which can be processed to find structure–attribute relationships,

[A]

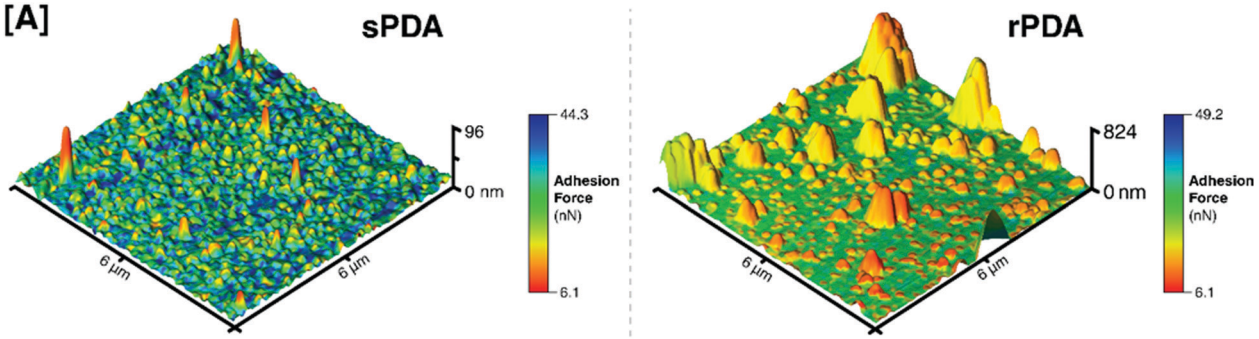

[B]

Properties	sPDA			rPDA		
	Interaggregate	Aggregate	Global	Interaggregate	Aggregate	Global
Stiffness (N/m)	1.9 ± 0.1	1.9 ± 0.1	1.9 ± 0.19	2.0 ± 0.2	1.9 ± 0.1	2.0 ± 0.1
Young's Modulus[a] (GPa)	2.6 ± 3.1	8.4 ± 1.6	5.2 ± 3.7	3.5 ± 2.9	7.8 ± 2.3	6.7 ± 4.0
Adhesion Force (nN)	35.7 ± 6.5	7.6 ± 0.8	22.7 ± 15.3	37.4 ± 7.6	7.6 ± 0.8	24.6 ± 16.3
Detachment Energy (nJ)	1057 ± 354	57.0 ± 10.8	595 ± 576	1162 ± 445	56.9 ± 10.7	688 ± 655
Hysteresis (nJ)	5.8 ± 1.2	6.35 ± 1.4	5.9 ± 1.9	5.9 ± 1.3	6.6 ± 1.6	6.3 ± 2.7
Compliance (N/m)	0.53 ± 0.03	0.57 ± 0.02	0.54 ± 0.03	0.54 ± 0.03	0.57 ± 0.02	0.54 ± 0.03
Hardness (MPa)	22.4 ± 0.9	20.9 ± 0.7	21.7 ± 0.8	21.2 ± 0.6	20.9 ± 0.7	21.1 ± 0.6

[a] Measured using the DMT model which takes work of adhesion into consideration

Fig. 2 [A] DPFM-AFM micrographs of sPDA and rPDA, showing variations in the adhesion force in relation to topographical features. [B] Summary of quantified nanomechanical properties.

both mathematically and visually, as exemplified by the topographical maps with an overlay of tip–surface adhesion strength (Fig. 2A). The average stiffness, hysteresis (a parameter associated with energy dissipation due to plastic deformation),[37] hardness and compliance (the ratio between the maximum indentation force and the maximum indentation value) were found to be consistent for the aggregates and underlying inter-aggregate regions for both PDA surfaces (Fig. 2B). In addition, we determined Young's modulus by using the DMT method due to the significant contribution of adhesive forces in the model.[53] Aggregates on both surfaces showed a substantially higher elastic modulus (sPDA: 8.4 GPa; rPDA: 7.8 GPa) than their respective underlying film (sPDA: 2.6 GPa; rPDA: 3.5 GPa). Comparatively, the elastic modulus of the films is on the lower range of common polymers, similar to that of polymethylmethacrylate (PMMA, 2.4 GPa), while the aggregates are in the middle of the previously reported range of PDA surfaces (4.3–10.5 GPa).[29,54] Accordingly, the global Young's modulus (calculated by including both inter-aggregate regions and individual aggregates) of the rPDA (6.7 GPa) was found to be greater than sPDA (4.8 GPa) which we suggest is a result of greater proportion of the surface composed of aggregates *versus* film.

For the first time, significant differences between inter-aggregate regions ("IAR"), which are typically the regions of interest in previous work, and the aggregates ("AGG") were detected for both adhesion force and detachment energy (Fig. 2A and B). In fact, regardless of the PDA condition, the force required to detach the tip from the underlying film and the associated detachment energy were found to be substantially greater when compared to aggregates. In fact, compared to aggregates, detachment from the sPDA film required 471% more force (IAR_{sPDA}: 35.7 nN; AGG_{sPDA}: 7.6 nN) and 1854% more energy (IAR_{sPDA}: 1057 nJ; AGG_{sPDA}: 56.98 nJ). Similar results were found on rPDA with film detachment requiring 493% more force (IAR_{rPDA}: 37.37 nN; AGG_{rPDA}: 7.6 nN) and 2040% more energy *versus* aggregates (IAR_{rPDA}: 1162.4 nN; AGG_{rPDA}: 57 nN). These results indicate that altering the proportion of aggregate, *versus* inter-aggregate film, may contribute to the overall adhesive potential of the surface both at the micrometric and nanometric scale. Specifically, the differential adhesion may affect the adsorptive capacity of the surface which in turn can influence the immobilization and accumulation of sera protein – an aspect which is well known to play a critical role in the interplay between cells and biomaterials.[55,56] Tuning of the PDA surface, through aggregate structure and prevalence, may then in turn allow for better control of chemical cueing (*e.g.*, targeted adsorption) or in generalized applications where PDA is used as a bioadhesive.[15,16,57,58]

Surface chemistry and wettability

X-ray photoelectron spectroscopy (XPS) and Raman imaging were used to assess the chemical composition and molecular conformation of PDA coatings. In particular, we aimed at determining whether the variation of an experimental parameter (*i.e.*, stirring) during deposition influenced the chemical properties of the resultant coatings, as seen in the case of temperature variations.[45] XPS survey spectra and high-resolution signatures from C 1s, O 1s and N 1s regions were collected and analyzed (Fig. 3A). Functional group peaks and energies are listed in Fig. 3B. The C 1s signal detected in bare borosilicate glass was assumed to be due to carbon contamination and was disregarded. The three observed major carbon peaks noted in Fig. 3B are consistent with previous literature.[39] N 1s regions were analyzed in ways to resolve the primary ($R\text{-}NH_2$), secondary (R-NH-R) and tertiary/aromatic (=N-R) amines. Each class of amine has been associated with either PDA (primary, secondary) or its intermediates (secondary, tertiary) with functional group dominance being shown to change with deposition time and reaction conditions.[39,44] In particular, primary amines have been associated with unreacted DA, and are most prevalent at very short deposition periods (<2 minutes). The formation of intermediates and subsequent polymer in later timepoints lead to a proportional transition toward secondary (predominant) and tertiary amines.[39] Because of the longer deposition time, sPDA and rPDA surfaces showed a minimal presence of primary amines. However, in contrast with previous literature, we detected a higher proportion of tertiary/aromatic amines when compared to secondary amines. We hypothesize this is due to the choice of Tris buffer as the solvent in our deposition series, *versus* the bicarbonate buffer previously used.[39] Evidence supporting this supposition has been recently reported,[44] and demonstrates that the chosen solvent critically impacts the predominance of terminal amines. Although results from this study still show secondary amines as the most prevalent, the dominance of tertiary/aromatic amines in our samples can be best explained by the use of comparatively high concentrations of Tris (25 mM *vs.* 10 mM) which may increase the opportunity for nitrogen in Tris to covalently bind to the quinone groups of the polymeric surface.[59] Additional differences may be attributed to the wettability and chemistry of the underlying surface which can affect PDA deposition.[60] We then focused on O 1s regions in ways to resolve the two primary peaks representing alcohol (C–O), associated with the C–OH of catechol groups and indoles, and carbonyl (C=O), associated with the structure of quinones. Our results show a predominance of hydroxyl over carbonyl functional groups. This is in line with literature that used Tris as a reaction buffer and can be best explained by the conversion of intermediate quinone carbonyl groups to indole hydroxyl groups during the covalent binding of Tris amino groups (*e.g.*, 5,6-indolequinone → 5,6-dihydroxyindole).[44]

In the case of Raman analysis, spectral deconvolution allowed to identify the specific bands that make up the characteristic signature of PDA in the 900–1600 cm^{-1} region (Fig. 3C and D). Of note, spectra collected on rPDA substrates displayed an evident decrease in the relative intensity of the band at 1370 cm^{-1}, associated to the C–N–C stretching in the indole aromatic ring. This may be due to an increased prevalence of the DHI intermediate in aggregate structures, which we showed to be considerably greater in size and number on the rPDA surfaces. This hypothesis is supported by recent work by Lyu *et al.* (2019) which indicates that aggregates may result from the copolymerization of DHI and uncyclized dopamine intermediates,

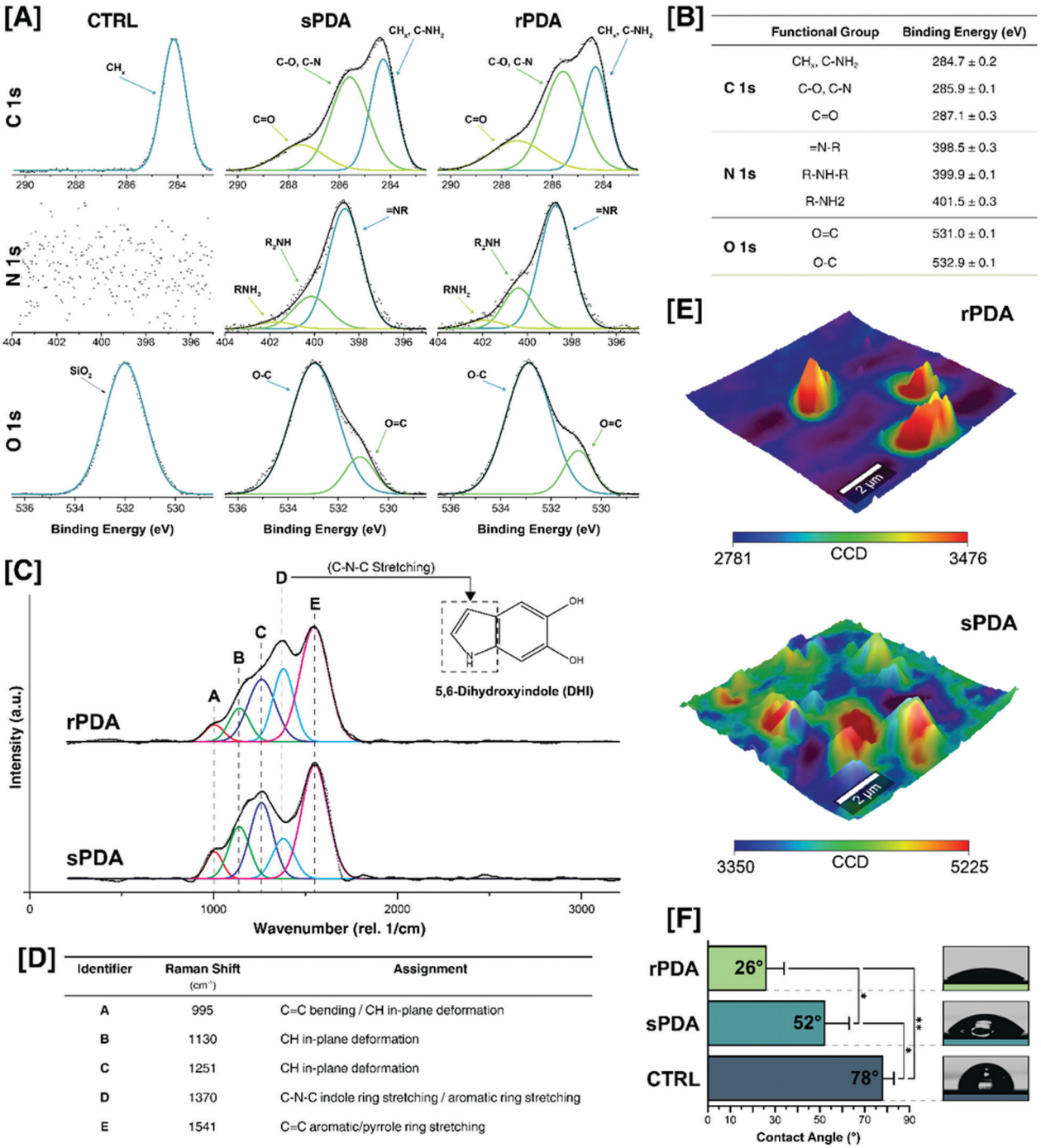

Fig. 3 [A] XPS spectra of glass CTRL, sPDA and rPDA. [B] XPS binding energy assignment. [C] Representative Raman spectrum of rPDA and sPDA. [D] Raman band assignment. [E] AFM-Raman overlay to display the correlation between variations in the benzene ring stretching modes (800–1800 cm^{-1}) and morphological features. [F] Contact angle goniometry measurements.

as opposed to the underlying film that is largely composed of PDA.[61]

The Raman signature of the dopamine molecule was also used to map out the chemical composition of PDA coatings to (i) ensure that the deposited films were homogeneously distributed on the glass coverslip and (ii) highlight any potential compositional alterations across the surface. By superimposing Raman maps over AFM topographical images, we validated the presence of a continuous film with localized Raman band intensity enhancement in correspondence of surface aggregates due to the localized accumulation of polymerized PDA to form the aggregates (Fig. 3E).

Surface topography and chemical composition are parameters known to affect wettability of surfaces.[62] Since XPS data show a consistent surface chemistry for both surfaces, we carried out contact angle measurements to assess whether

the morphological differences between rPDA and sPDA affected wettability. In agreement with previous work, sPDA surfaces presented with substantially decreased static contact angle when compared to the 78° of bare glass coverslips.[22,63] Of note, contact angle values decreased to 26° on rPDA (Fig. 3F). While values for classically deposited PDA (sPDA) are consistent with previously published values (ranging 50° to 70°, depending on the underlying substrate), rPDA coatings have a notably larger contact angle.[27] Differences in the experimental set—up during rotational deposition, including speed variability and the use of a shaking *versus* rotational platform, are thought to contribute to these discrepancies. Although the initial concentration of PDA during deposition and thickness of the film has been shown to not affect surface energy, the presence of larger structures at the nano- and micro-scales are believed to result in enhanced Wenzel homogeneous wetting due to the improved immersion of the droplet in the asperities of the surface.[64]

Cellular results

To assess the bioactive effects of PDA and whether they are modulated by the deposition method, we carried out *in vitro* immunofluorescent imaging of bone marrow-derived hMSCs on controls and PDA surfaces at various time points.

Cell morphology. At 1 h of culture, hMSCs seeded on both PDA surfaces displayed advanced cell spreading morphologies, when compared to control. Respectively, the morphology for cells on sPDA and rPDA was predominantly protrusive (62.1% *vs.* 56.4%) followed by elongated (13% *vs.* 29.7%) (Fig. 4A and B). Interestingly, while control surfaces had the greatest comparative proportion of cells being of early circular stage (26.3%) compared to sPDA (9.9%) and rPDA (6.8%), they also possessed the greatest share of the advanced elongated morphology with 13.6% *versus* 3.1% and 3.7% for sPDA and rPDA, respectively. At 4 h, the development of a well-spread morphology on rPDA becomes evident, with 68.2% of cells showing the most advanced multipolar morphology, greater than that observed on sPDA (41.8%) and on control surfaces (5.2%), respectively. The relative proportion of the next most advanced morphology, namely multipodal, was statistically similar between sPDA (34.5%) and rPDA (27.2%). Conversely, the multipodal proportion in control surfaces (42.9%) was significantly greater than both PDA surfaces. Notably, all cells on rPDA surfaces progressed beyond the initial spherical and circular morphologies after 4 hours, indicating that adequate cell–substrate signaling (*e.g.*, integrin clustering) was generated across the population in order to progress to later morphologies.

The surface properties of biomaterials, including stiffness and micro-/nano-topography, directly affect the activation of integrin-ECM binding groups which play a role in the kinetics of spreading and motility.[54,65] Once initiated, cells undergo a fast period of quick isotropic spreading characterized by lower centripetal actin flow indicative of low projection formation,[66] which contributes to the development of a circular morphology. Subsequently, the cells undergo anisotropic spreading through a sequence of stochastic, transient extension periods (STEPs) that results in high centripetal actin flow due to peripheral projection formation,[66] which translates into a protrusive morphology. These generalized processes, in combination with resultant substrate-induced cell structure formation, will produce whole cell morphology changes that can be quantitatively analyzed to better understand cell–substrate relationships. To this end, using post-processing of fluorescence microscopy images in a custom Cellprofiler pipeline, cell area, perimeter, form factor and compactness were quantified. Notably, although these are stringent geometrical descriptors to quantify cell shape, they cannot help to discern differences for those morphologies similarly characterized by jagged contours and irregular filopodial protrusions (*i.e.*, protrusive, multipodal and multipolar morphology) (Fig. 4A). The complexity of the contour and the presence of irregular cellular protrusions (Fig. 4B) may in fact yield similar values in terms of area, perimeter and form factor in cells belonging to different morphological categories. For this reason, data interpretation of the quantitative characterization (Fig. 4C and D) should not be dissociated from the morphological classification (Fig. 4A). This is particularly critical during the early stages of adhesion (1 and 4 hours) where cellular changes are more rapid.

At 1 hour (Fig. 4C), hMSCs adhering on sPDA and rPDA surfaces exhibited a significantly more spread morphology than that of cells on control surfaces with 94% and 95% greater relative area, respectively. As expected with enhancement in cell area, cells on PDA surfaces had also significantly larger perimeters. Intriguingly, although cells on sPDA and rPDA had insignificant differences in cell area, the perimeter was found to be dissimilar. In fact, when compared to control surfaces, cells on sPDA and rPDA had perimeter enhancement of 34.1% and 77.6%, respectively. This likely derives from the predominance of cells characterized by more jagged contours. Our results also indicate that substantial cell populations on sPDA and rPDA are either undergoing, or have largely completed, early stage isotropic spreading which is responsible for rapid area increases, explaining the similarity in cell area.[66] The 32.5% difference in cells with a multipolar morphology between PDA samples (Fig. 4A) can be best explained by the increase in protrusive morphologies in rPDA, indicating a greater proportion of the rPDA population undergoing the anisotropic STEPs process, which is characterized by minimal area changes but large perimeter variations reflective of plasma membrane protrusions.[66–68] This is further confirmed by the decrease in form factor for rPDA cells, compared to the control, which indicates less circular cells. Notably, form factor and compactness did not display significant differences on PDA surfaces.

At 4 hours (Fig. 4D), differences in cell area, perimeter and form factor are offset. However, cells on rPDA showed a significantly greater degree of compactness which is indicative of a more irregular morphology, akin to that seen in multipolar morphologies which were predominant in the earlier morphological analysis at this time point. In this context, the elongated morphologies may be correlated to the generation of cell

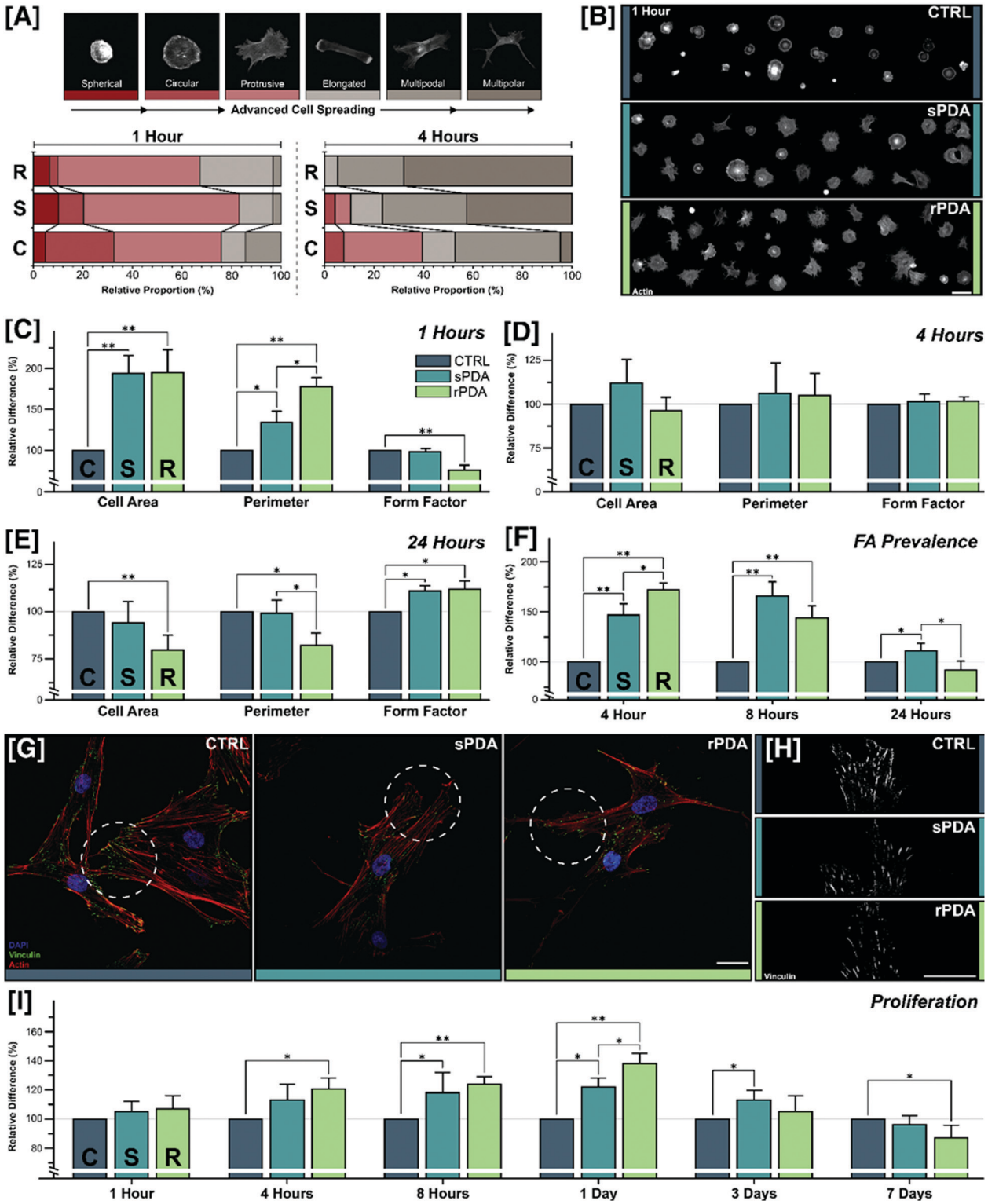

Fig. 4 [A] Legend of morphologies exhibited through the advancement of cell spreading with correlated colour bars (top). Relative proportions of morphologies categorized from hMSCs incubated in serum-containing media and seeded on CTRL (C), sPDA (S) and rPDA (R) surfaces. [B] Fluorescence images showing the presence of different morphologies of hMSCs adhering on respective surfaces after 1 h. Scale bar = 100 μm. Quantitative morphological parameters at [C] 1 h, [D] 4 h and [E] 24 h. [F] Focal adhesion prevalence in the first 24 hours. Results are expressed as percentage increase/decrease in respect to untreated controls (C). ANOVA: $*P < 0.05$; $**P < 0.01$. [G] Confocal fluorescence images of focal adhesion complexes (vinculin), actin and nuclei. Scale bar = 25 μm. [H] Higher magnification confocal fluorescence images of only focal adhesions. Scale bar = 25 μm. [I] hMSCs proliferation expressed as percentage difference in respect to untreated controls (C). ANOVA: $*P < 0.05$; $**P < 0.01$.

traction forces throughout the cell body *via* actin stress fibers which is the result of focal adhesion maturity.[69]

At 24 hours (Fig. 4E), cells on rPDA presented with a significant decrease (−19.3%) in comparative size to control surfaces. These differences were not significant between PDA surfaces. The observed reduction in cell area on rPDA is believed to be due to the transition to late stage morphologies (*e.g.*, multipolar) which are characterized by a more contracted structure. In this context, Rac1-dependent recruitment of Myosin IIA and subsequent actinomyosin mediated contraction during adherence and late stage spreading is indicative of the onset of cell traction forces which translate into polarization and initiation of migratory behavior.[70–72] This is further supported by the significant decrease in perimeter in rPDA *versus* both sPDA and control surfaces, which likely stems from the retraction of multiple podia in favor of polarization with the lamella rich front and contracted rear, indicative of a migratory cell responding to environmental physicochemical cues.[73] Important to note is that the form factor of cells on sPDA and rPDA, while both significantly higher and therefore less circular than the control, are statistically similar. This indicates that differences in cell area and perimeter resulting from cell body contraction in rPDA are uniform in aspect. Taken together, our results suggest that rPDA surfaces are superior to sPDA surfaces in the promotion of advanced cell spreading, indicating a surface that is increasingly capable of generating meaningful integrin-mediated cell–substrate adhesions that translate downstream into earlier productive traction force *via* the actin cytoskeleton. As such, initiation of subsequent cell functions, such as the expression of cyclin D1 for the progression of the cell cycle, can begin earlier and may be further promoted in ways that have yet to be studied (*e.g.*, post-migratory influence on protein expression for enhanced bioactivity including differentiation).[74]

Focal adhesions (“FAs”). To better understand the dynamics of focal adhesions in PDA bioactivity, we utilized indirect immunofluorescence to label for the vinculin protein, an early member of the focal adhesion complex (Fig. 4F). At 1 h, the contracted morphology of early stage cell spreading resulted in substantial stacking of out-of-focus light and subsequently led to the inability to confidently discern smaller focal complexes and adhesions on all surfaces. As a result, this timepoint was omitted from analysis. At 4 h, both PDA surfaces showed a remarkably significant elevation in the number of focal adhesions compared to control surfaces with sPDA at +47% and rPDA at +72%. Between PDA samples, rPDA had a significant 17% lead over sPDA, a trend that continued into the 8 h time point, with sPDA and rPDA presenting with +66% and +44% more focal adhesions than control. Of note, the lead that rPDA had over sPDA diminished. At 24 h, rPDA was found to have a considerable −17% lag behind sPDA though it was indistinguishable from control surfaces. sPDA on the other hand retained a lessened but still significant +11% lead over control surfaces. An example of cells at 24 h can be seen in Fig. 4G and H.

The adhesion of a cell to synthetic (*e.g.*, biomaterials) and natural (*e.g.*, extracellular matrix) substrates is regulated by transmembrane integrin-mediated multimeric protein complexes which link the extracellular environment to internal cytoskeletal structures enabling the process of mechanotransduction.[75] Early stage focal complexes (~0.5 μm in length) indicate initial integrin activation and aggregation, forming transient supramolecular complexes, and may undergo maturation into focal adhesions (1–5 μm in length) in response to adequate stimulation, namely RhoA activity.[76] These highly dynamic structures, critical in the initial interaction with the cellular micro-environment, will form in response to physicochemical stimuli (*e.g.*, microtopography, surface stiffness). The establishment of FAs in turn directs cell behavior, and therefore it is a critical aspect in the investigation of cell–substrate interactions.[77] In this context, the rapid increase in PDA focal adhesion formation in early timepoints is believed to be the result of activation and clustering of integrin α5β1.[29,78] The sheer prevalence of the adhesions is an indication of effective generation of cell–substrate interactions, which have undergone productive force transduction through myosin-II mediated contractile forces, and implies the presence of superior physicochemical stimuli.[70,79,80]

When taking into consideration the morphological and cell structure data, the reduction in focal adhesion prevalence in the PDA surfaces, namely rPDA, is suggestive of late stage cell spreading and is indicative of a cell entering motility. During the transition to motility, focal adhesions around the periphery of the cell undergo pruning and stress fiber orientation in favor of polarization resulting in a highly dynamic leading lamellipodium and less dynamic rear retracting edge.[81,82] As such, taken together with the morphological and structural data, these results suggest that by 24 hour, rPDA surfaces support populations of cells that are at later stages of motility. The comparative decrease between 8 h and 24 h for sPDA implies the transition to motility as well. Combined data for the control surfaces, however, indicate that the cells are less able to create productive cell–substrate interactions and as such are in earlier stages of cell spreading and/or may be less motile.

Cell number. Cell count is a hallmark of effective bioactive surfaces and is an indicator of its clinical potential (*e.g.*, osseointegration of orthopedic implants). In an effort to investigate the differential proliferative capability of PDA surfaces, we carried out culturing experiments that extended over a week (Fig. 4I). Within the first 4 h, rPDA surfaces showed a significant 20.5% increase in proliferative ability, compared to control surfaces, while sPDA surfaces remained similar. By 8 h, the proliferative ability of rPDA over control surfaces becomes much more evident with a significant rise in relative proliferation (+23.7%). Of note, it is not discernible from sPDA surfaces which were similarly found to be different from control surfaces (+18.2%). With respect to control surfaces, cells on rPDA increased their proliferative induction to a significant +38%, with sPDA following closely behind with +22.2%. At this point, the PDA surfaces can first be seen to be statistically different with a significant +13.1% in proliferative effect of rPDA over sPDA. Intriguingly, over the following 6 days, the number of cells on rPDA underwent a substantial reduction with a significant

−11% decrease after 7 days of culture with respect to the control surfaces, despite after 3 days of culture sPDA surfaces retained their significant 13% elevation.

PDA coatings have long been explored for their ability to enhance cellular viability and cell proliferation for a variety of applications, ranging from revascularization with endothelial cells and scaffolding for cartilage tissue engineering to ceramic enhancement coatings for osteoblasts and cryogel scaffold for stem cell therapy.[29,83–85] As of yet, the mechanism to which PDA coatings elicit these cytocompatible and proliferative effects is not fully understood: major limitations in generalized models derive from the high degree of variability between the PDA surfaces being studied, with differences stemming from key variables including the deposition method, solvent choice and underlying base substrate. As such, the ability to control for multiple variables while manipulating an experimental characteristic (*i.e.*, topography) provides a framework to better understand the mechanism of action with the potential for additional insight into its other noted effects.

Cell proliferation was measured through the fixation and fluorescent imaging of stained hMSCs cultured in serum-containing media over the course of the first 7 d post-seeding. The larger variance in cell number on sPDA surfaces at 4 h and 8 h may indicate heterogeneous progression of spreading and downstream cell cycle initiation between populations on the surface, a theory that is reinforced by the morphological analysis. As cellular adhesion is affected by the cell cycle and the stage the cell is in at the time of seeding,[86] heterogeneity may be reduced in the future by use of a temporary cell cycle arresting compound (*e.g.*, cytochalasin D for G1-S).[87] At 24 hours we see marked differences between the surfaces.

Generalized explanation for the advancement of cell proliferation by PDA samples is still inconclusive with most work incomparably based on developed substrates and studied cell lines. Luo *et al.*, (2013) determined that for endothelial cells, the proliferative capability may be associated with the surface quinone content which was enhanced with thermal treatment and subsequently producing greater viability.[88] However, in our case, XPS results indicated no significant difference in functional groups associated with elevated catechol presence on rPDA *versus* sPDA. It is also possible that the proliferative ability is dependent on enhanced serum protein pre-adsorption. A study by Zhou *et al.* (2014) found that when comparing the standard deposition method with a rapidly depositing shaking method at similar deposition times, the BSA binding ability was indistinguishable.[45] In addition, previous work from our group has indicated no differences in adsorptive capacity between modified titanium and PDA coated titanium despite considerable bioactive enhancement in spreading and proliferation which extended beyond three dimensions.[29] Although it has been suggested that cell spreading and proliferation are mainly dependent on surface chemistry while cell elongation and morphology is topography driven (*e.g.*, grooves), our results indicate that given differential proliferation on PDA surfaces of similar chemistry and differing topography, physicochemical characteristics do play a major role in the proliferative inductive capability of PDA.[78]

Of unique interest is the reduction of relative proliferation in rPDA surfaces after 3 and 7 days which were unexpected due to previous results in our lab with MG63 proliferation showing advancement beyond the third day of culture with no substantial reduction.[29] An explanation may be the amplified inductive capacity of rPDA for osteogenic differentiation with PDA in general having been well described and utilized in a variety of methods.[89–91] The osteogenic potential of PDA has been correlated to the promotion of integrin clustering and activation of subsequent PI3K signaling pathways.[92] PI3K signaling is enabled by FAK activity at established focal adhesions which in turn has been found to stimulate osteogenic differentiation of hMSCs through ERK-dependent pathways.[93] Thereby rPDA, which we have shown to promote cell spreading and focal adhesion formation, may in turn promote the FAK/PI3K/ERK mediated osteogenic differentiation of hMSCs which is known to have an antagonistic relationship with cell proliferation.[94] Terminal differentiation is correlated to a reduction, and sometimes complete exit, from the cell cycle.

The lack of osteogenic induction by control surfaces allows for the retention of proliferation rates of the non-differentiated hMSCs, which in combination with the potential reduction in cell cycle progression of differentiated cells in rPDA, may explain the relative drop off by the third and seventh day. This may be supported by the relative decreases in sPDA surfaces at these timepoints which follow a similar, though lagging, trend and may be indicative of the reduced, though present, osteogenic inductive abilities of sPDA.

Filopodial projections. SEM imaging qualitatively revealed that filopodial projections sprouting from hMSCs were more numerous on both PDA surfaces, and that they directly interacted with PDA aggregates (Fig. 5). While the hMSCs did interact to some degree with larger aggregates on both PDA surfaces (Fig. 5B and C), further observation showed that filopodia generated plasma membrane envelopes over specific aggregates (Fig. 5G and H). Of note on the rPDA surface, where plasma membrane projections were more numerous, the extensions were seen to navigate around certain sizes of aggregates prior to the enveloping of the features (Fig. 5H). This suggests that filopodia may have a preference for terminal interactions with aggregates of a critical size or aspect (*e.g.*, mechanical property). Although there were greater numbers of projections on the rPDA surface, these appeared to be shorter than those on the sPDA, which may suggest that the abundance of the surface polymeric features may satisfy cellular criteria for interaction. The clear majority of projections extending from cells on sPDA appeared to be unbound to surface aggregates. Together, this work indicates that cells interact directly with both PDA aggregates and surface features, where certain features are preferentially interacted with (possibly due to size) and result in the development of membrane sheathes which indicate reinforcement of cell-feature adhesion and interaction.

The osteogenic properties of PDA coatings[89,95,96] were confirmed with OSX staining at 7 days (data not shown). While both

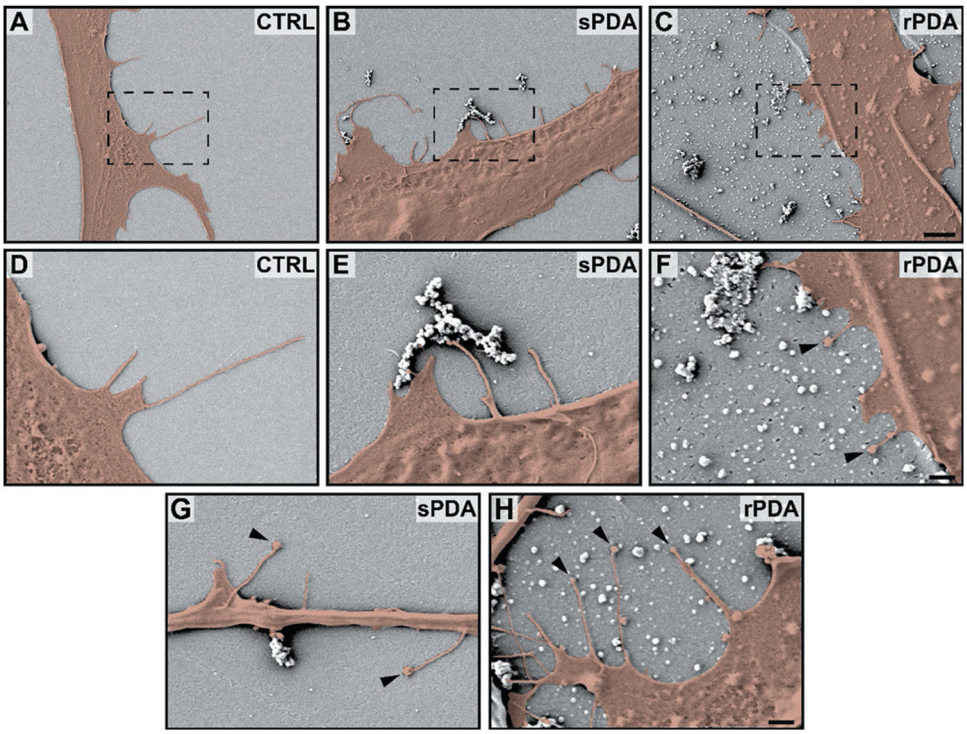

Fig. 5 [A–C] Low magnification SEM images of hMSCs seeded on control and PDA surfaces. Lines visible in [C] are most likely defects (*e.g.*, microcracks, polishing marks, scratches) in the underlying glass substrate which yielded a localized accumulation of PDA, as previously reported in the case of mechanically polished titanium.[29] Scale bar = 1 μm. [D–F] High magnification SEM images of projections from hMSCs. Scale bar = 4 μm. [G and H] Representative images of projections from hMSCs that interact with features on sPDA and rPDA surfaces. Scale bar = 4 μm.

PDA surfaces showed greater nuclear localization (*vs.* control), indicating greater osteogenic differentiation, no clear differences were detected between the respective PDA surfaces by confocal imaging. However, morphological differences that are correlated to osteogenic differentiation[97] were observed between PDA surfaces at 7 days and subsequently warrants future investigation by means of longitudinal genomic methods (*e.g.*, qPCR).

Serum independent component (SIC). The benefit of PDA with respect to its interaction with sera protein has been suggested to be due to the ability of PDA to stabilize adsorbed protein and prevent denaturation.[27] Although previous work by Tsai *et al.* (2011) intended to investigate the serum-free aspect of PDA by culturing in serum-free *versus* serum-containing media, their approach introduced the critical confound of circulating sera protein, which is well-known to have an essential role in the stimulation, growth and activity of cells in culture.[84] To improve upon this concept, we aimed at singling out the contribution of the adhesion properties *versus* intrinsic cueing of PDA by carrying out cellular experiments in serum-free conditions. To this end, hMSCs were serum-starved overnight prior to seeding on respective surfaces pretreated in serum-containing or serum-free media for 6 h. Cells were successively cultured for 1 and 4 hours (Fig. 6) without the addition of FBS in the medium. To qualitatively confirm the efficacy of pre-treatment in serum-containing media, we carried out ATR-FTIR measurements which demonstrated the presence of a protein adlayer on all surfaces (Fig. S1, ESI†). These findings are corroborated by our previous work where we employed ATR-FTIR and liquid chromatography mass spectroscopy to investigate adsorbed proteins on sPDA coatings after incubation for 6 hours in α-MEM + 10% FBS solution.[29] Given the lack of indication that the surface chemistry between sPDA and rPDA are critically different, we can thus consider protein adsorption to be similar between these two surfaces.

In order to permit the detection and quantification of a serum-independent component (SIC) in a straightforward manner, the SIC was assessed by calculating the ratio of a quantitative descriptor (*i.e.*, morphology, spreading and proliferation) on pre-adsorbed (PA) surfaces over non-preadsorbed (NPA) surfaces.

After 1 h and 4 h (Fig. 6A), hMSCs plated on control and PDA samples were imaged and categorized into one of the six spreading morphologies used with normal culturing conditions (Fig. 4A). At 1 h, cells on NPA surfaces were found to be primarily protrusive in nature on sPDA (72%) and rPDA (68%) surfaces, while circular cells were the clear majority in control (66%) surfaces. Cells on rPDA surfaces, when compared to sPDA, showed a substantial increase in the proportion of the more advanced elongated (14.5% *vs.* 7.2%) and multipodal (6.8% *vs.* 3.6%) morphologies. When comparing the NPA and PA conditions, similar inter-sample differences were seen, with rPDA eliciting more advanced spreading morphologies. In general, the pre-adsorption of serum proteins further progressed cell spreading morphologies when compared to the respective

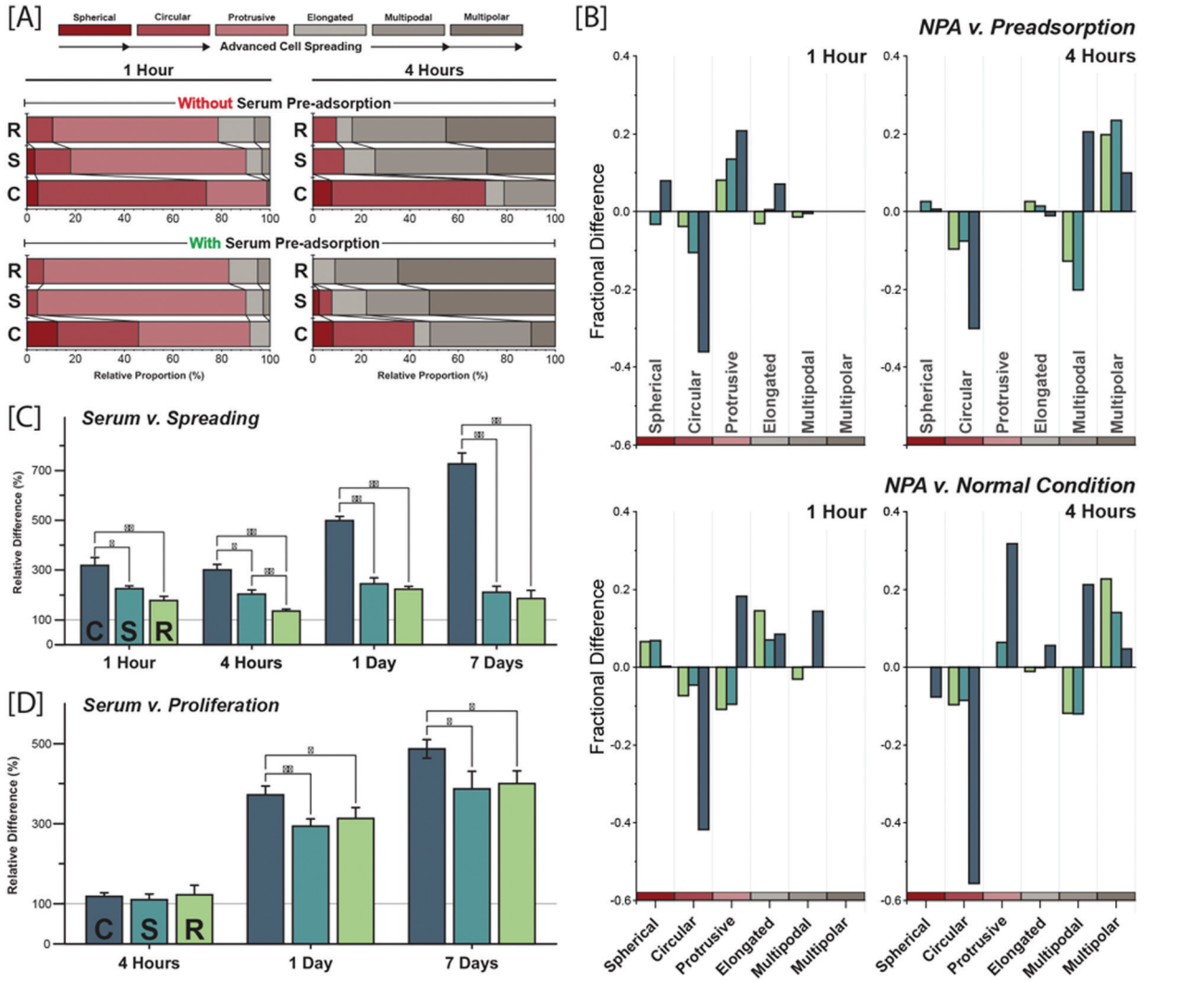

Fig. 6 [A] Legend of morphologies exhibited through the advancement of cell spreading with correlated colour bars (top). Relative proportions of hMSCs morphologies after incubation in serum-free media on controls (C), sPDA (S) and rPDA (R) surfaces with and without pre-treatment in serum containing media. [B] Comparative quantification of morphological differences associated with protein pre-adsorption (top) and the presence of medium in the culture medium (bottom). Serum independent component (SIC) effect size for [C] cell spreading and [D] proliferation. Effect size is calculated as the dividend of the respective measure (*e.g.*, proliferation) from preadsorbed samples over non-preadsorbed samples. ANOVA: $*P < 0.05$; $**P < 0.01$.

non-pre-adsorbed surface. At 4 h, cells adhering on PDA surfaces continued to show increasingly progressed morphologies, compared to controls, with similar trends to those at 1 h. Under non-pre-adsorption, PDA surfaces exhibited most cells on sPDA and rPDA with either multipodal (46% *vs.* 38%) and multipolar (28% *vs.* 45%) morphology. On control samples, there was an absence of multipolar cells with the majority of cells being circular (63%) followed by multipodal (21%). These trends continued in the preadsorbed condition, with a significant 52% reduction in circular cells on control samples and an 87% increase in multipodal cells. By comparing standard (Fig. 4A) and serum-free culturing conditions on PA substrates (Fig. 6A, bottom) we can infer the effects of serum on cellular morphology under the assumption that protein adsorption in these two cases yields a similar surface-bound adlayer. This hypothesis is plausible since in standard cultures, serum protein adsorption occurs almost instantaneously, and this can thus be regarded to as a pre-treatment of surfaces with serum proteins prior to cell cultures. At 1 h, on all surfaces the absence of serum causes an increase of cells with the protrusive morphology at the expense of more advanced spreading. However, at 4 h, this effect is mitigated by the presence of the pre-adsorbed protein adlayer, since cells on all surfaces show a similar distribution with minimal differences towards more advanced spreading morphologies. This observation about the compensating role of pre-adsorbed serum proteins is in agreement with previous work that showed that the co-immobilization of growth factors on gelatin substrates permits to maintain the morphology of hMSCs in a serum-free medium.[98] In order to quantitatively expand on the effects of serum proteins, both surface-bound and in the culture medium, we expressed the morphology distribution obtained on NPA conditions in relation

to that obtained on PA and normal conditions, respectively (Fig. 6B). It can be readily observed that at 1 h and 4 h the presence of serum proteins on the surface (Fig. 6B, top) and in the medium (Fig. 6B, bottom) similarly leads to a marked reduction in the circular morphologies (particularly evident for the control surface) and to a corresponding increase of well-spread morphologies such as protrusive and multipodal. Taken together, although the impact is less evident for the PDA substrates, there is still an important role played by serum whether in the medium or adsorbed on the surface.

In terms of spreading (Fig. 6C), within the first hour the pre-adsorption of serum proteins amounted to a +218% enhancement in cell spreading on glass and was found to be statistically different to the effect size of sPDA (+126%) and rPDA (+78%). There was no difference in effect detected between PDA samples at this time point. At 4 h, these statistical differences continued, with control surfaces showing a +306% enhancement in spreading followed by +113% and +37% on sPDA and rPDA surfaces, respectively. Notably, protein pre-adsorption was found to have a significantly greater effect on sPDA *versus* rPDA. At 24 h, a significant enhancement in effect size was found on CTRL surfaces (+388%). sPDA and rPDA surfaces had statistically similar effect sizes of 144% and 135%, respectively. Similar trends extended throughout the first week of culture with CTRL surfaces showing a furthered effect size at +634% whereas sPDA and rPDA were unchanged and statistically similar to each other.

In terms of cell proliferation (Fig. 6D), at 4 h, no significant differences were detected. At 24 h, the effect size on all surfaces increase with enhancements of +272%, +194% and +213% detected for control, sPDA and rPDA surfaces, respectively. The effect size on control surfaces was found to be statistically higher than the sPDA and rPDA (however no differences were detected between PDA surfaces). By day 7, these statistical relationships continue with pre-adsorptive effects of +388%, +293% and +301%, measured on control, sPDA and rPDA surfaces, respectively.

Taken together, on all samples and timepoints, cells on rPDA surfaces displayed significantly advanced cell morphologies when compared to sPDA and control surfaces in serum-free cultures. Herein, we have confirmed that even under serum independent conditions, PDA surfaces enhance the spreading of cells, further adding evidence to a serum independent component. In comparison to normal culturing conditions, at 1 h there is a remarkable decrease in protrusive morphologies, which are indicative of anisotropic spreading, and is in agreement with Dubin-Thaler *et al.* (2004) whom indicated that serum deprivation promotes isotropic spreading.[66] Although this particular morphology is hindered, the deprivation of circulating serum does not seem to retard the transition to later morphologies at future timepoints. Consequently, this reduction in transient anisotropic spreading in combination with the low proportions of spherical and circular morphologies, in both NPA and PA conditions, indicates that PDA surfaces are capable of generating cell–substrate adhesions that result in quicker spreading initiation and morphological transitions, instead of relying more heavily on the stochastic environmental sensing of STEPs. It has been proposed in multiple studies that the primary mechanism of action for PDA bioactivity is tied to its adsorptive capacity, despite little consideration taken to inter-study control for physicochemical traits (*e.g.*, aggregate size, distribution).[27,84] Our results clearly show that although serum pre-adsorption positively impacts morphological progression, as expected, the absence of protein adlayer does not lead to a critical loss of cell spreading especially in rPDA surfaces. This indicates that regardless of chemically similarity and adsorption condition, rPDA possess additional features (*e.g.*, topography) that can further sustain the initial behavior of cells beyond that of the classically deposited sPDA.

Conclusion

In this work, we focused on (i) determining how treatment parameters influence the physiochemical makeup of PDA surfaces, (ii) assessing how PDA surfaces influence stem cell behavior and (iii) confirming and investigating the SIC of PDA effect. While there have been many studies investigating the bioactivity of PDA, inconsistent control for variables (*e.g.*, deposition method) and lack of advanced surface analysis could limit their inter-study comparison power. For this reason, we aimed at providing a detailed investigation from the morphological, nanomechanical and chemical point of view to provide the field with additional physicochemical insights for future studies with PDA. Results from this study show that rPDA surfaces, though chemically similar to sPDA, possess a higher degree of wettability associated with the presence of surface-bound and scattered micro-/nano-scale particles resulting in elevated roughness. Through discrimination of PDA aggregates *versus* the underlying film, we were able to characterize the novel differences in physical characteristics, namely the fact that 1845% more energy and 381% more force is required to detach from PDA films *versus* aggregates. This in turn led to the global reduction in required detachment force and energy in rPDA surfaces, due to the ubiquity of large aggregates over the surface. This reduction in required forces may impact the ability for cells to readily generate and collapse adhesions associated with the generation of traction force as seen during spreading and motility.

Cellular assays provided insight into the degree to which the physical differences between PDA surfaces can be attributed to differences in bioactivity. Our results have shown that despite chemical similarity, rPDA surfaces induce advanced spreading morphologies, confirmed through structural and focal adhesion analysis, at earlier timepoints beyond that of classically deposited PDA. In addition, rPDA presented elevated cell proliferation in the first 24 h, an effect that was diminished in the first 7 d which may be indicative of differentiation. This elevated bioactivity, coupled with the previously reported enhancement of antibacterial activity, provides further evidence to support the use of rPDA has a bioactive coating for orthopedic and dental implants.

The second part of this study was to confirm the existence of a serum-independent component to PDA, a variable that has been largely unconsidered and overshadowed by the adsorptive capacity of the polymer. We have confirmed that there is in fact a SIC of PDA that plays a role on cell spreading and proliferation of hMSCs over the first 7 d of cell culture. Of note, in cell spreading, the effect size of pre-adsorption remained relatively consistent for PDA surfaces throughout timepoints, whereas under proliferation, the effect size of the SIC increased over time. This indicates that PDA surfaces contain a serum independent effect that is consistent in its promotion of cell spreading over time, whereas still evident in proliferation studies, the SIC plays a lesser role. As such, these analyses suggest that the differences between sPDA and rPDA surfaces in normal cell culture conditions are not a direct result of differences in respective SICs, suggesting any differences are the result of variables other than the surface chemistry and adsorptive capacity.

In summary, this study provided novel insight into the physicochemical attributes of sPDA and rPDA coatings. In addition, cellular analyses between them provided context to their differential bioactive effects. We have also confirmed the existence of a serum independent component of PDA coatings which is shown to play a major role in cellular adhesion and less so in proliferation. Our results provide new evidence supporting the use of rPDA has a biomaterials interface while contributing to the further understanding of the mechanisms behind PDA bioactivity which may impact and influence the reasoning of both past and future PDA-based studies.

Conflicts of interest

There are no conflicts of interest to declare.

Acknowledgements

We acknowledge Mrs Ryan Berthelot for critical reading of the manuscript and David Lomboni for his help with ATR-FTIR measurements. This work was supported by the Natural Sciences and Engineering Research Council (NSERC) through the Discovery grant, by the Canada Foundation for Innovation (CFI) and the Ontario Ministry of Research and Innovation (MRI) through the Leaders of Opportunity (LOF) fund. The authors acknowledge the resources and assistance provided by the Cell Biology and Image Acquisition (CBIA).

Notes and references

1 A. T. Nguyen, S. R. Sathe and E. K. F. Yim, *J. Phys.: Condens. Matter*, 2016, **28**, 183001.
2 F. Guilak, D. M. Cohen, B. T. Estes, J. M. Gimble, W. Liedtke and C. S. Chen, *Cell Stem Cell*, 2009, **5**, 17–26.
3 A. M. Schaap-Oziemlak, P. T. Kühn, T. G. Van Kooten and P. Van Rijn, *RSC Adv.*, 2014, **4**, 53307–53320.
4 M. Gasik, *Sci. Technol. Adv. Mater.*, 2017, **18**, 550–562.
5 J. M. Morais, F. Papadimitrakopoulos and D. J. Burgess, *AAPS J.*, 2010, **12**, 188–196.
6 A. Cipitria and M. Salmeron-Sanchez, *Adv. Healthcare Mater.*, 2017, 6.
7 M. N. Andalib, Y. Dzenis, H. J. Donahue and J. Y. Lim, *Biomater. Res.*, 2016, 20.
8 R. Sinha, M. Hoon, J. Baudin, H. Okawa, R. O. L. Wong and F. Rieke, *Cell*, 2017, **168**, 413–426.e12.
9 B. Bhushan, *Langmuir*, 2012, **28**, 1698–1714.
10 S. R. Coyer, A. Singh, D. W. Dumbauld, D. A. Calderwood, S. W. Craig, E. Delamarche and A. J. García, *J. Cell Sci.*, 2012, **125**, 5110–5123.
11 L. G. Griffith, *Annals of the New York Academy of Sciences*, New York Academy of Sciences, 2002, vol. 961, pp. 83–95.
12 K. E. Healy, A. Rezania and R. A. Stile, *Annals of the New York Academy of Sciences*, New York Academy of Sciences, 1999, vol. 875, pp. 24–35.
13 K. S. Straley, C. W. P. Foo and S. C. Heilshorn, *J. Neurotrauma*, 2010, **27**, 1–19.
14 H. Lee, S. M. Dellatore, W. M. Miller and P. B. Messersmith, *Science*, 2007, **318**, 426–430.
15 J. Ryu, S. H. Ku, H. Lee and C. B. Park, *Adv. Funct. Mater.*, 2010, **20**, 2132–2139.
16 P. Kord Forooshani and B. P. Lee, *J. Polym. Sci., Part A: Polym. Chem.*, 2017, **55**, 9–33.
17 S. He, P. Zhou, L. Wang, X. Xiong, Y. Zhang, Y. Deng and S. Wei, *J. R. Soc., Interface*, 2014, **11**, 20140169.
18 J. Xu, N. Xu, T. Zhou, X. Xiao, B. Gao, J. Fu and T. Zhang, *Surf. Coat. Technol.*, 2017, **320**, 608–613.
19 X. Chen, Y. Huang, G. Yang, J. Li, T. Wang, O. Schulz and L. Jennings, *Curr. Pharm. Des.*, 2015, **21**, 4262–4275.
20 P. Li, Z. Wang, W. Li, Y. Liu, J. Wang and S. Wang, *ACS Appl. Mater. Interfaces*, 2015, **7**, 15481–15493.
21 T. S. Sileika, H. Do Kim, P. Maniak and P. B. Messersmith, *ACS Appl. Mater. Interfaces*, 2011, **3**, 4602–4610.
22 L. Su, Y. Yu, Y. Zhao, F. Liang and X. Zhang, *Sci. Rep.*, 2016, **6**, 1–8.
23 S. H. Ku and C. B. Park, *Biomaterials*, 2010, **31**, 9431–9437.
24 S. Hong, K. Y. Kim, H. J. Wook, S. Y. Park, K. D. Lee, D. Y. Lee and H. Lee, *Nanomedicine*, 2011, **6**, 793–801.
25 K. C. L. Black, J. Yi, J. G. Rivera, D. C. Zelasko-Leon and P. B. Messersmith, *Nanomedicine*, 2013, **8**, 17–28.
26 J. Liu, H. Xu, X. Tang, J. Xu, Z. Jin, H. Li, S. Wang, J. Gou and X. Jin, *RSC Adv.*, 2017, **7**, 15864–15876.
27 S. H. Ku, J. Ryu, S. K. Hong, H. Lee and C. B. Park, *Biomaterials*, 2010, **31**, 2535–2541.
28 M. S. Lord, M. Foss and F. Besenbacher, *Nano Today*, 2010, **5**, 66–78.
29 A. J. Steeves, A. Atwal, S. C. Schock and F. Variola, *J. Mater. Chem. B*, 2016, **4**, 3145–3156.
30 X. Wei, X. Yang, Z. P. Han, F. F. Qu, L. Shao and Y. F. Shi, *Acta Pharmacol. Sin.*, 2013, **34**, 747–754.
31 D. C. Ding, Y. H. Chang, W. C. Shyu and S. Z. Lin, *Cell Transplant.*, 2015, **24**, 339–347.
32 B. D. Boyan, E. M. Lotz and Z. Schwartz, *Tissue Eng., Part A*, 2017, **23**, 1479–1489.

33 J. Galipeau and L. Sensébé, *Cell Stem Cell*, 2018, **22**, 824–833.
34 C. A. Schneider, W. S. Rasband and K. W. Eliceiri, *Nat. Methods*, 2012, **9**, 671–675.
35 J. Schindelin, I. Arganda-Carreras, E. Frise, V. Kaynig, M. Longair, T. Pietzsch, S. Preibisch, C. Rueden, S. Saalfeld, B. Schmid, J. Y. Tinevez, D. J. White, V. Hartenstein, K. Eliceiri, P. Tomancak and A. Cardona, *Nat. Methods*, 2012, **9**, 676–682.
36 D. Nečas and P. Klapetek, *Cent. Eur. J. Phys.*, 2012, **10**, 181–188.
37 C. A. Rezende, L. T. Lee and F. Galembeck, *Langmuir*, 2009, **25**, 9938–9946.
38 B. V. Derjaguin, V. M. Muller and Y. P. Toporov, *J. Colloid Interface Sci.*, 1975, **53**, 314–326.
39 R. A. Zangmeister, T. A. Morris and M. J. Tarlov, *Langmuir*, 2013, **29**, 8619–8628.
40 H. Wei, J. Ren, B. Han, L. Xu, L. Han and L. Jia, *Colloids Surf., B*, 2013, **110**, 22–28.
41 M. Baginska, B. J. Blaiszik, T. Rajh, N. R. Sottos and S. R. White, *J. Power Sources*, 2014, **269**, 735–739.
42 J. Feng, H. Fan, D. A. Zha, L. Wang and Z. Jin, *Langmuir*, 2016, **32**, 10377–10386.
43 A. E. Carpenter, T. R. Jones, M. R. Lamprecht, C. Clarke, I. H. Kang, O. Friman, D. A. Guertin, J. H. Chang, R. A. Lindquist, J. Moffat, P. Golland and D. M. Sabatini, *Genome Biol.*, 2006, **7**, R100.
44 K. Patel, N. Singh, J. Yadav, J. M. Nayak, S. K. Sahoo, J. Lata, D. Chand, S. Kumar and R. Kumar, *Phys. Chem. Chem. Phys.*, 2018, **20**, 5744–5755.
45 P. Zhou, Y. Deng, B. Lyu, R. Zhang, H. Zhang, H. Ma, Y. Lyu and S. Wei, *PLoS One*, 2014, **9**, e0113087.
46 M. J. P. Biggs, R. G. Richards and M. J. Dalby, *Nanomedicine*, 2010, **6**, 619–633.
47 E. Ngandu Mpoyi, M. Cantini, P. M. Reynolds, N. Gadegaard, M. J. Dalby and M. Salmerón-Sánchez, *ACS Nano*, 2016, **10**, 6638–6647.
48 M. A. Partridge and E. E. Marcantonio, *Mol. Biol. Cell*, 2006, **17**, 4237–4248.
49 M. Azatov, X. Sun, A. Suberi, J. T. Fourkas and A. Upadhyaya, *Phys. Biol.*, 2017, **14**, 065003.
50 G. Abagnale, M. Steger, V. H. Nguyen, N. Hersch, A. Sechi, S. Joussen, B. Denecke, R. Merkel, B. Hoffmann, A. Dreser, U. Schnakenberg, A. Gillner and W. Wagner, *Biomaterials*, 2015, **61**, 316–326.
51 M. Sun, G. Chi, P. Li, S. Lv, J. Xu, Z. Xu, Y. Xia, Y. Tan, J. Xu, L. Li and Y. Li, *Int. J. Med. Sci.*, 2018, **15**, 257–268.
52 R. G. Wells, *Hepatology*, 2008, **47**, 1394–1400.
53 B. Cappella, *Mechanical Properties of Polymers Measured through AFM Force-Distance Curves*, 2016.
54 Y. Liu, K. Ai and L. Lu, *Chem. Rev.*, 2014, **114**, 5057–5115.
55 C. J. Wilson, R. E. Clegg, D. I. Leavesley and M. J. Pearcy, *Tissue Eng.*, 2005, **11**, 1–18.
56 D. R. Absolom, W. Zingg and A. W. Neumann, *J. Biomed. Mater. Res.*, 1987, **21**, 161–171.
57 J. Cui, Y. Yan, G. K. Such, K. Liang, C. J. Ochs, A. Postma and F. Caruso, *Biomacromolecules*, 2012, **13**, 2225–2228.
58 Y. H. Ding, M. Floren and W. Tan, *Biosurf. Biotribol.*, 2016, **2**, 121–136.
59 N. F. Della Vecchia, R. Avolio, M. Alfè, M. E. Errico, A. Napolitano and M. D'Ischia, *Adv. Funct. Mater.*, 2013, **23**, 1331–1340.
60 C. Zhang, L. Gong, L. Xiang, Y. Du, W. Hu, H. Zeng and Z. K. Xu, *ACS Appl. Mater. Interfaces*, 2017, **9**, 30943–30950.
61 Q. Lyu, N. Hsueh and C. L. L. Chai, *Langmuir*, 2019, **35**, 5191–5201.
62 M. E. Kavousanakis, N. T. Chamakos and A. G. Papathanasiou, *J. Phys. Chem. C*, 2015, **119**, 15056–15066.
63 J. Jiang, L. Zhu, L. Zhu, B. Zhu and Y. Xu, *Langmuir*, 2011, **27**, 14180–14187.
64 V. Ball, D. Del Frari, V. Toniazzo and D. Ruch, *J. Colloid Interface Sci.*, 2012, **386**, 366–372.
65 C. M. Lo, H. B. Wang, M. Dembo and Y. L. Wang, *Biophys. J.*, 2000, **79**, 144–152.
66 B. J. Dubin-Thaler, G. Giannone, H. G. Döbereiner and M. P. Sheetz, *Biophys. J.*, 2004, **86**, 1794–1806.
67 C. A. Reinhart-King, M. Dembo and D. A. Hammer, *Biophys. J.*, 2005, **89**, 676–689.
68 E. Kassianidou, D. Probst, J. Jäger, S. Lee, A. Lou Roguet, U. S. Schwarz and S. Kumar, *Cell Rep.*, 2019, **27**, 1897–1909.e4.
69 A. Livne and B. Geiger, *J. Cell Sci.*, 2016, **129**, 1293–1304.
70 A. M. Pasapera, S. V. Plotnikov, R. S. Fischer, L. B. Case, T. T. Egelhoff and C. M. Waterman, *Curr. Biol.*, 2015, **25**, 175–186.
71 T. Wakatsuki, R. B. Wysolmerski and E. L. Elson, *J. Cell Sci.*, 2003, **116**, 1617–1625.
72 J. C. Kuo, *J. Cell. Mol. Med.*, 2013, **17**, 704–712.
73 L. Smith, S. Cho and D. E. Discher, *Semin. Cell Dev. Biol.*, 2017, **71**, 84–98.
74 K. L. Watts, E. Cottrell, P. R. Hoban and M. A. Spiteri, *Respir. Res.*, 2006, **15**, 88.
75 E. A. Cavalcanti-Adam, T. Volberg, A. Micoulet, H. Kessler, B. Geiger and J. P. Spatz, *Biophys. J.*, 2007, **92**, 2964–2974.
76 M. A. Wozniak, K. Modzelewska, L. Kwong and P. J. Keely, *Biochim. Biophys. Acta, Mol. Cell Res.*, 2004, **1692**, 103–119.
77 L. E. McNamara, R. Burchmore, M. O. Riehle, P. Herzyk, M. J. P. Biggs, C. D. W. Wilkinson, A. S. G. Curtis and M. J. Dalby, *Biomaterials*, 2012, **33**, 2835–2847.
78 J. L. Wang, K. F. Ren, H. Chang, F. Jia, B. C. Li, Y. Ji and J. Ji, *Macromol. Biosci.*, 2013, **13**, 483–493.
79 H. Wolfenson, T. Iskratsch and M. P. Sheetz, *Biophys. J.*, 2015, **107**, 2508–2514.
80 H. B. Schiller and R. Fässler, *EMBO Rep.*, 2013, **14**, 509–519.
81 D. H. Kim and D. Wirtz, *FASEB J.*, 2013, **27**, 1351–1361.
82 C. C. Zimmer, L. Shi, Y. Shih, J. Li, L. Jin, S. Lo and G. Liu, *Sci. China: Chem.*, 2012, **55**, 1922–1930.
83 W. Zhou, X. Xiao, M. Cai and L. Yang, *Nano Lett.*, 2014, **14**, 5250–5256.
84 W. B. Tsai, W. T. Chen, H. W. Chien, W. H. Kuo and M. J. Wang, *Acta Biomater.*, 2011, **7**, 4187–4194.
85 A. Jemat, M. J. Ghazali, M. Razali and Y. Otsuka, *Biomed. Res. Int.*, 2015, 2015.

86 M. C. Jones, J. A. Askari, J. D. Humphries and M. J. Humphries, *J. Cell Biol.*, 2018, **217**, 3203–3218.
87 G. Chen and X. Deng, *Bio-Protoc.*, 2018, **8**, e2994.
88 R. Luo, L. Tang, S. Zhong, Z. Yang, J. Wang, Y. Weng, Q. Tu, C. Jiang and N. Huang, *ACS Appl. Mater. Interfaces*, 2013, **5**, 1704–1714.
89 D. J. Lee, Y. T. Lee, R. Zou, R. Daniel and C. C. Ko, *Sci. Rep.*, 2017, **7**, 12984.
90 C. Wu, W. Fan, J. Chang and Y. Xiao, *J. Mater. Chem.*, 2011, **21**, 18300–18307.
91 R. Xue, J. Y. S. Li, Y. Yeh, L. Yang and S. Chien, *J. Orthop. Res.*, 2013, **31**, 1360–1365.
92 J. J. Lee, I. S. Park, G. S. Shin, S. K. Lyu, S. G. Ahn, T. S. Bae and M. H. Lee, *Int. J. Precis. Eng. Manuf.*, 2014, **15**, 1647–1655.
93 R. M. Salasznyk, R. F. Klees, W. A. Williams, A. Boskey and G. E. Plopper, *Exp. Cell Res.*, 2007, **313**, 22–37.
94 S. Ruijtenberg and S. van den Heuvel, *Cell Cycle*, 2016, **15**, 196–212.
95 J. S. Lee, J. K. Yi, S. Y. An and J. S. Heo, *Cell. Physiol. Biochem.*, 2014, **34**, 1824–1834.
96 L. Li, Y. Li, L. Yang, F. Yu, K. Zhang, J. Jin, J. Shi, L. Zhu, H. Liang, X. Wang and Q. Jiang, *Ann. Transl. Med.*, 2019, **7**, 240–254.
97 F. Matsuoka, I. Takeuchi, H. Agata, H. Kagami, H. Shiono, Y. Kiyota, H. Honda and R. Kato, *PLoS One*, 2013, **8**, e55082.
98 H. Mao, S. Min Kim, M. Ueki and Y. Ito, *J. Mater. Chem. B*, 2017, **5**, 928–934.